



Contents lists available at ScienceDirect

## Medical Image Analysis

journal homepage: www.elsevier.com/locate/media



# Prototypical few-shot segmentation for cross-institution male pelvic structures with spatial registration

Yiwen Li<sup>a,\*</sup>, Yunguan Fu<sup>b,c</sup>, Iani J.M.B. Gayo<sup>b</sup>, Qianye Yang<sup>b</sup>, Zhe Min<sup>b</sup>, Shaheer U. Saeed<sup>b</sup>, Wen Yan<sup>b,g</sup>, Yipei Wang<sup>d</sup>, J. Alison Noble<sup>d</sup>, Mark Emberton<sup>e</sup>, Matthew J. Clarkson<sup>b</sup>, Henkjan Huisman<sup>f</sup>, Dean C. Barratt<sup>b</sup>, Victor A. Prisacariu<sup>a</sup>, Yipeng Hu<sup>b,d</sup>

 $\bigcirc^a$ Active Vision Laboratory, Department of Engineering Science, University of Oxford, Oxford, U.K.

🔐 Department of Medical Physics and Biomedical Engineering, UCL Centre for Medical Image Computing, and Wellcome / EPSRC Centre for Interventional and Surgical Sciences, University College London, London, U.K.
cInstaDeep Ltd., London, U.K.

 $\bigcirc$  Institute of Biomedical Engineering, Department of Engineering Science, University of Oxford, Oxford, UK

 $^{
u}$ Division of Surgery & Interventional Science, University College London, London, U.K.

<sup>f</sup>Department of Radiology, Radboud University Nijmegen Medical Centre, Nijmegen, The Netherlands

BDepartment of Electrical Engineering, City University of Hong Kong, Hong Kong, China

Keywords: few-shot learning, multi-class segmentation, image registration, pelvic

## ABSTRACT

The prowess that makes few-shot learning desirable in medical image analysis is the efficient use of the *support* image data, which are labelled to classify or segment new classes, a task that otherwise requires substantially more training images and expert annotations. This work describes a fully 3D prototypical few-shot segmentation algorithm, such that the trained networks can be effectively adapted to clinically interesting structures that are absent in training, using only a few labelled images from a different institute. First, to compensate for the widely recognised spatial variability between institutions in episodic adaptation of novel classes, a novel spatial registration mechanism is integrated into prototypical learning, consisting of a segmentation head and an spatial alignment module. Second, to assist the training with observed imperfect alignment, support mask conditioning module is proposed to further utilise the annotation available from the support images. Extensive experiments are presented in an application of segmenting eight anatomical structures important for interventional planning, using a data set of 589 pelvic T2-weighted MR images, acquired at seven institutes. The results demonstrate the efficacy in each of the 3D formulation, the spatial registration, and the support mask conditioning, all of which made positive contributions independently or collectively. Compared with the previously proposed 2D alternatives, the few-shot segmentation performance was improved with statistical significance, regardless whether the support data come from the same or different institutes.

© 2022 Elsevier B. V. All rights reserved.

## 1. Introduction

Multi-structure segmentation is one of the fundamental computing tasks in medical imaging applications, found in diagno-

\*Corresponding author: E-mail: yiwen.li@st-annes.ox.ac.uk

sis, treatment, and monitoring, and remains a research interest. Diagnosis of varieties of diseases can be assisted by quantifying the morphology, or its change, of multiple structures. For example, brain disorders, including Alzheimer's disease (Petrella et al., 2003) and Parkinson (Hutchinson and Raff, 2000), associates with abnormal volumes or shapes of neurological regions. Identifying brain structures is the key to many quantitative studies, such as functional activation mapping and brain development analysis (Han and Fischl, 2007). Minimally invasive treatments often benefit from careful planning of both interventional instruments and guidance imaging, with respect to segmented patient-specific anatomical structures. In endoscopic pancreatobiliary procedures, as previously reported, image guidance that displays registered anatomical models outside the endoscopic field of view helps the surgeon during targeting and navigation (Howe and Matsuoka, 1999).

This work is primarily concerned with segmenting multiple organs and urologically interesting structures on T2-weighted MR images from prostate cancer patients, to plan targeted biopsy, focal therapy, and, increasingly, other therapeutic procedures such as radiotherapy. Accurate segmentation of these structures help with targeting suspected cancerous regions found in multiparametric MR imaging with respect to the prostate gland and avoiding vulnerable surrounding structures, such as rectum, bladder and neurovascular bundles, for minimising risks in infection, impotence and other potential injury and complications (De la Rosette et al., 2010).

The data-driven representation learning enabled by deep neural networks has led to promising segmentation results in multi-structure segmentation tasks, for example, in neuroimaging (Henschel et al., 2020) and abdominal organs (Weston et al., 2019). Automating this task reduces the current requirement of manual segmentation which is often associated with costs in expertise and intra- and inter-observer variations (Fiorino et al., 1998). However, recent supervised segmentation methods mostly rely on large data sets with full annotations, subject to the similar limitations in labelling, albeit only with training. On the other hand, few-shot image learning aims to classify unseen classes using only a few labelled examples (Snell et al., 2017; Sung et al., 2018). For medical image segmentation, such novel classes may represent new types of organ or anatomical regions, whose expert annotations are not available for large training data sets. Using our intended interventional planning application as an example, different biopsy or therapy procedures may require different anatomical structures and pathological regions to be annotated during the planning stage. Prostate zonal structures, if not routinely segmented for MR-planning of radiotherapy, may provide more precise target localisation in registration-assisted ultrasound-guided focal ablation or a new therapy.

The now well-recognised performance loss in cross-institute generalisation of deep learning models (Gibson et al., 2018) has motivated a body of research such as domain adaptation (Ren et al., 2018; Meyer et al., 2021) and federated learning (Li et al., 2021a). This work focuses on few-shot segmentation with the practically important cross-institution context (as shown in Fig. 1), which aims to segment a *novel class* from a *query* image, given only a few *support* images and their binary masks of the novel class, from a *novel institution* where the limited labelled data are available. In other words, the model should be able to simultaneously adapt to both novel classes and novel institutions.

To improve the inter-class and inter-institute generalisation,

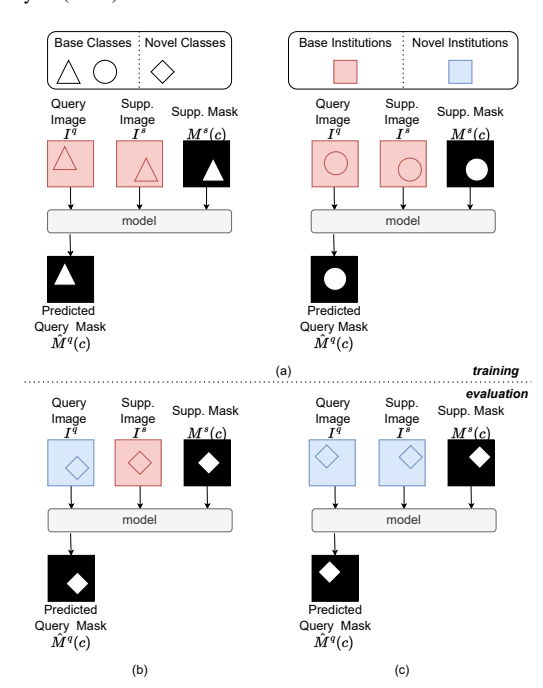


Fig. 1. Visualisation of the proposed cross-institution few-shot segmentation task. As shown in (a), the task aims to train a model on the base data set including images from base institutions with corresponding masks on base classes and generalise to novel institution as well as novel classes. The model is evaluated on segmenting novel classes from query images acquired by novel institutions, while support images comes from either base or novel institutions, respectively shown in (b) and (c).

this work first examines the manifestation of the performancereducing inter-institute variability in prototypical few-shot image segmentation algorithms. In particular, we investigate the impact of spatial alignment, or the lack thereof, between support and query data from different institutes, a key component in such prototypical learning paradigm, on the few-shot segmentation accuracy.

First, addressing one of the previously identified challenges of spatial inconsistency (Tian et al., 2020), also found in medical image applications (Guo et al., 2021; Sun et al., 2022), we develop a *spatial registration mechanism* to align the support and query images prior to the comparison between the two. This spatial registration mechanism consists of a *segmentation head* and a *spatial alignment module*, trained end-to-end, and is motivated by medical-image-specific observations of the difference between intra- and inter-institution data characteristics, due to different scanners and local imaging protocols, discussed further in Section 4.4.

Second, we propose an additional *support mask conditioning module*, also trained end-to-end, to enforce the conditioning on the available novel class labels. The conditioning module is empirically designed to work together with the spatial registration mechanism, to maximise utilisation of the few and prized support masks.

In addition to the evaluation of efficacy due to each proposed component, this work also demonstrates the benefit of the proposed 3D formulation, replacing existing 2D neural network-based few-shot segmentation approaches (Feyjie et al., 2020; Ouyang et al., 2020; Roy et al., 2020; Abdel-Basset et al., 2021;

Guo et al., 2021; Tang et al., 2021; Yu et al., 2021; Sun et al., 2022).

One widely identified problem in both developing and evaluating multi-structure segmentation algorithms is the lack of a sizable labelled data set. To the date of submission of this paper, there were no multi-structure annotations publicly available for pelvic MR images. Through this work, all of our manual labels from open data sets have been made available at https://zenodo.org/record/7013610, for aiding the reproducibility of this work and, potentially, for other urologic or radiologic tasks concerning multiple pelvic anatomical structures

Our preliminary results were recently presented (Li et al., 2022), contributions from this paper include 1) a more detailed description and discussion of the spatial registration mechanism, 2) a new support mask conditioning module, 3) a substantially larger and fully labelled data set, and 4) more ablation comparison experiments. These are also summarised as follows.

- We introduced the cross-institution few-shot segmentation task to address the data scarcity problem specifically faced in medical applications.
- We proposed the first 3D neural network for prototypical few-shot multi-class segmentation, which requires fewer parameters while achieving state-of-the-art performance.
- We developed an spatial registration mechanism and a support mask conditioning module, directly addressing the observed limitations in medical image few-shot segmentation, for improving generalisation across data from different institutions.
- We presented extensive ablation studies to investigate the impact of the proposed individual components, the increasing number of support data, the varying size of the training set, and the permutations in the available institutes.
- We published all expert annotations based on public image data sets at https://zenodo.org/record/7013610, which includes full segmentation of eight distinctive male lower pelvic structures in 589 3D MR images.
- The code implementing the proposed algorithms has also been made publicly available at https://github.com/kate-sann5100/CrossInstitutionFewShotSegmentation.

## 2. Related Work

## 2.1. Few-shot segmentation

The few-shot segmentation task was first introduced in computer vision applications (Shaban et al., 2017) where the goal is to segment the *novel class* in a *query* image in the presence of a few *support* images having the same class labelled. Using episodic training which takes both query and support images as input, Shaban et al. (2017) demonstrated a better performance

compared to the common fine-tuning methods, which fine-tunes the models on the support images per novel class. In 2018, Dong and Xing (2018) proposed prototypical episode learning that represents the novel class in the support image with a single *prototype* vector and compares it with query features to perform segmentation. This strategy was later adopted in many further research works (Zhang et al., 2019; Liu et al., 2020; Li et al., 2021b).

Due to the common challenges in data collection, few-shot segmentation was also adapted to different medical images, including CT (Roy et al., 2020), MRI (Mondal et al., 2018), ultrasound (Guo et al., 2021), etc. The early methods applied finetuning strategy and addressed the over-fitting on support images with multi-tasking (Mondal et al., 2018; Cui et al., 2020) and data augmentation (Zhao et al., 2019; He et al., 2020; Wang et al., 2021). Roy et al. (2020) was one of the first that adopted prototypical learning in medical imaging, reporting promising performance. Ouyang et al. (2020) and Yu et al. (2021) extracted multiple prototype vectors and performed a locationguided comparison, with the assumption of similar spatial layouts between the query and support images. However, in crossinstitution scenarios, regions of interest may be located differently between queries and supports, as shown in Fig. 10. In this work, we proposed an integrated spatial registration mechanism to address such inconsistency.

In addition to data scarcity, higher-dimensional data in medical imaging often poses practical challenges in neural network training. Roy et al. (2020) proposed to use 2D neural networks, that pre-trained on large data sets such as ImageNet, and performed slice-by-slice inference when applied to 3D medical images. This strategy was also adopted by most of the following prototypical methods (Feyjie et al., 2020; Ouyang et al., 2020; Abdel-Basset et al., 2021; Guo et al., 2021; Tang et al., 2021; Yu et al., 2021; Sun et al., 2022) except Kim et al. (2021), which integrated a bidirectional gated recurrent unit (Cho et al., 2014) to process 2D features extracted from adjacent slices.

To the best of our knowledge, there has been no prior work that successfully deployed 3D neural networks that receive and output 3D image volumes directly, using prototypical training for few-shot segmentation in medical imaging applications. Investigating the 3D formulation is not only technically interesting, but may also lead to potentially superior performance and/or efficiency in this inherently 3D segmentation task.

## 2.2. Cross-institution learning

The proposed cross-institution few-shot segmentation task aims to segment a novel class in images from a novel institution, with support images and labels from the same novel or other non-novel institutions. Although the objective is also to generalise on novel data, it differs from federated learning and domain adaptation due to their constraints on data privacy, accessibility, and availability. However, an optimal gain in efficient use of labelled data could be achieved by combining these methods with few-shot learning.

Federated learning is a learning paradigm that targets the problem of data governance and privacy by training algorithms collaboratively without the need for physically exchanging the data themselves, sometimes requiring the compliance of varying access policy (Rieke et al., 2020). It has been used in different medical imaging applications (Li et al., 2021a), but the focus is mainly on improving performance in trained classes without the need for generalisation in a novel class.

There exist three different domain adaptation methods: supervised, unsupervised, and semi-supervised. While sharing the same overarching objective, i.e. generalising to new domains such as novel classes, the supervised domain adaptation (Hosseini-Asl et al., 2016) does not explicitly focus on the data scarcity as few-shot learning. Unsupervised methods (Perone et al., 2019), on the other hand, often assume large-scale data set from the novel institution but without labels, thus paying a different attention from that of cross-institution few-shot learning. Combining both techniques, semi-supervised methods (Fu et al., 2019; Xia et al., 2020) can leverage labelled and unlabelled data sets more efficiently.

Despite the distinct focuses, techniques and methodologies from federated learning and domain adaptation have indeed been considered in developing our cross-institute few-shot segmentation approach. For example, the spatial normalisation and divergence between features have commonly been adopted in federated learning (Li et al., 2020) and feature-level domain adaptation (Tomar et al., 2021), respectively.

## 3. The Cross-Institution Few-Shot Segmentation Task

Consider a set of classes and institutions, C and  $\mathcal{U}$ , respectively. For each institution  $u \in \mathcal{U}$ ,  $I_u$  denotes the set of all images. All classes have been segmented for each image: given a class  $c \in C$ ,  $M(I_u, c)$  represents the corresponding mask for the image  $I_u \in \mathcal{I}_u$  from the institution u.

The classes C and the institutions  $\mathcal{U}$  are split into disjoint sets  $(C_{\text{base}}, C_{\text{novel}})$  and  $(\mathcal{U}_{\text{base}}, \mathcal{U}_{\text{novel}})$ , respectively. The images  $I_u$  of each institution u are also separated into disjoint training and test subsets  $I_u^{\text{train}}$  and  $I_u^{\text{test}}$ . A base data set  $\mathcal{D}_{\text{base}}$  is formed with training images and the corresponding labels of the base classes from all the base institutions.

$$\mathcal{D}_{\text{base}} = \bigcup_{u \in \mathcal{U}_{\text{base}}} \bigcup_{I \in \mathcal{I}^{\text{train}}} \bigcup_{c \in C_{\text{base}}} \{ (I, M(I, c)) \}. \tag{1}$$

Similarly, test images and the corresponding labels of novel classes from all base institutions form another data set,

$$\mathcal{D}_{\text{base\_ins\_novel\_cls}} = \bigcup_{u \in \mathcal{U}_{\text{base\_}}} \bigcup_{I \in I^{\text{test}}} \bigcup_{c \in C_{\text{novel}}} \{ (I, M(I, c)) \}, \quad (2)$$

together with the data set of images from the novel institutions and the novel classes' labels,

$$\mathcal{D}_{\text{novel\_ins\_novel\_cls}} = \bigcup_{u \in \mathcal{U}_{\text{novel}}} \bigcup_{I \in I_u} \bigcup_{c \in C_{\text{novel}}} \{ (I, M(I, c)) \}, \quad (3)$$

a novel data set is built focusing on novel classes:

$$\mathcal{D}_{\text{novel}} = \mathcal{D}_{\text{base\_ins\_novel\_cls}} \cup \mathcal{D}_{\text{novel\_ins\_novel\_cls}}.$$
 (4)

Therefore, the cross-institution segmentation task aims to train a model on the base data set  $\mathcal{D}_{\text{base}}$  and generalise to the novel data set  $\mathcal{D}_{novel}$  which contains novel classes on both base and novel institutions. Specifically, following the few-shot setting described in Roy et al. (2020) and Ouyang et al. (2020), the model is tasked to segment a novel class  $c \in C_{novel}$  in a query image  $I_u^q$  acquired from a novel institution  $u \in \mathcal{U}_{novel}$  with only K support examples  $\{(I_{u^s,k}^s, M(I_{u^s,k}^s, c))\}_{k=1}^K$  from the same or different institutions. The predicted query mask  $\hat{M}(I_u^q, c)$  is compared with the label  $M(I_u^q, c)$  with a segmentation metric such as the Dice score (Sudre et al., 2017). Such evaluation procedure is named an *episode* with K-shot, which is also detailed in Algorithm 1.

```
Algorithm 1: Evaluation Procedure
   Input: Neural network \phi_{\theta} with parameters \theta
                             Images I_u^{\text{test}} for all base institutions u \in \mathcal{U}_{base}
                            Images I_u for all novel institutions u \in \mathcal{U}_{novel}
                            Masks for all novel classes in C_{novel}
   Output: Dice scores for all, novel, and base institutions:
                            ALL_DICE, NOVEL_DICE, and BASE_DICE
   ALL_DICE_SUM = 0
   ALL_DICE_COUNT = 0
   NOVEL\_DICE\_SUM = 0
   NOVEL_DICE_COUNT = 0
   BASE\_DICE\_SUM = 0
   BASE\_DICE\_COUNT = 0
   for I^q \in \bigcup_{u \in \mathcal{U}_{novel}} \mathcal{I}_u do
             for u \in \mathcal{U}_{novel} do
                        Sample I^s \in \mathcal{I}_u, such that I^s \neq I^q
                        for c \in C_{novel} do
                                  Denote the mask of c in I^s as M^s(c)
                                  Denote the mask of c in I^q as M^q(c)
                                  Predict \hat{M}^q(c) = \phi_{\theta}(I^q, I^s, M^s(c))
                                  Evaluate dice = Dice(\hat{M}^q(c), M^q(c))
                                  Update ALL_DICE_SUM += dice
                                  Update ALL_DICE_COUNT += 1
                                  Update NOVEL_DICE_SUM += dice
                                  Update NOVEL_DICE_COUNT += 1
                       end
             end
             for u \in \mathcal{U}_{base} do
                        Sample I^s \in \mathcal{I}_u^{test}
                        for c \in C_{novel} do
                                  Denote the mask of c in I^s as M^s(c)
                                  Denote the mask of c in I^q as M^q(c)
                                  Predict \hat{M}^q(c) = \phi_{\theta}(I^q, I^s, M^s(c))
                                  Evaluate dice = Dice(\hat{M}^q(c), M^q(c))
                                  Update ALL_DICE_SUM += dice
                                  Update ALL_DICE_COUNT += 1
                                  Update BASE_DICE_SUM += dice
                                  Update BASE_DICE_COUNT += 1
                        end
             end
   end
  Compute ALL_DICE = ALL_DICE_SUM ALL_DICE_COUNT
Compute NOVEL_DICE = NOVEL_DICE_SUM NOVEL_DICE_COUNT
Compute BASE_DICE = BASE_DICE_SUM
BASE_DICE_SUM
COMPUTE BASE_DICE_SUM
BASE_DICE_SUM
COMPUTE BASE_D
```

Compute BASE\_DICE =  $\frac{BASE\_DICE\_SUM}{BASE\_DICE\_COUNT}$ 

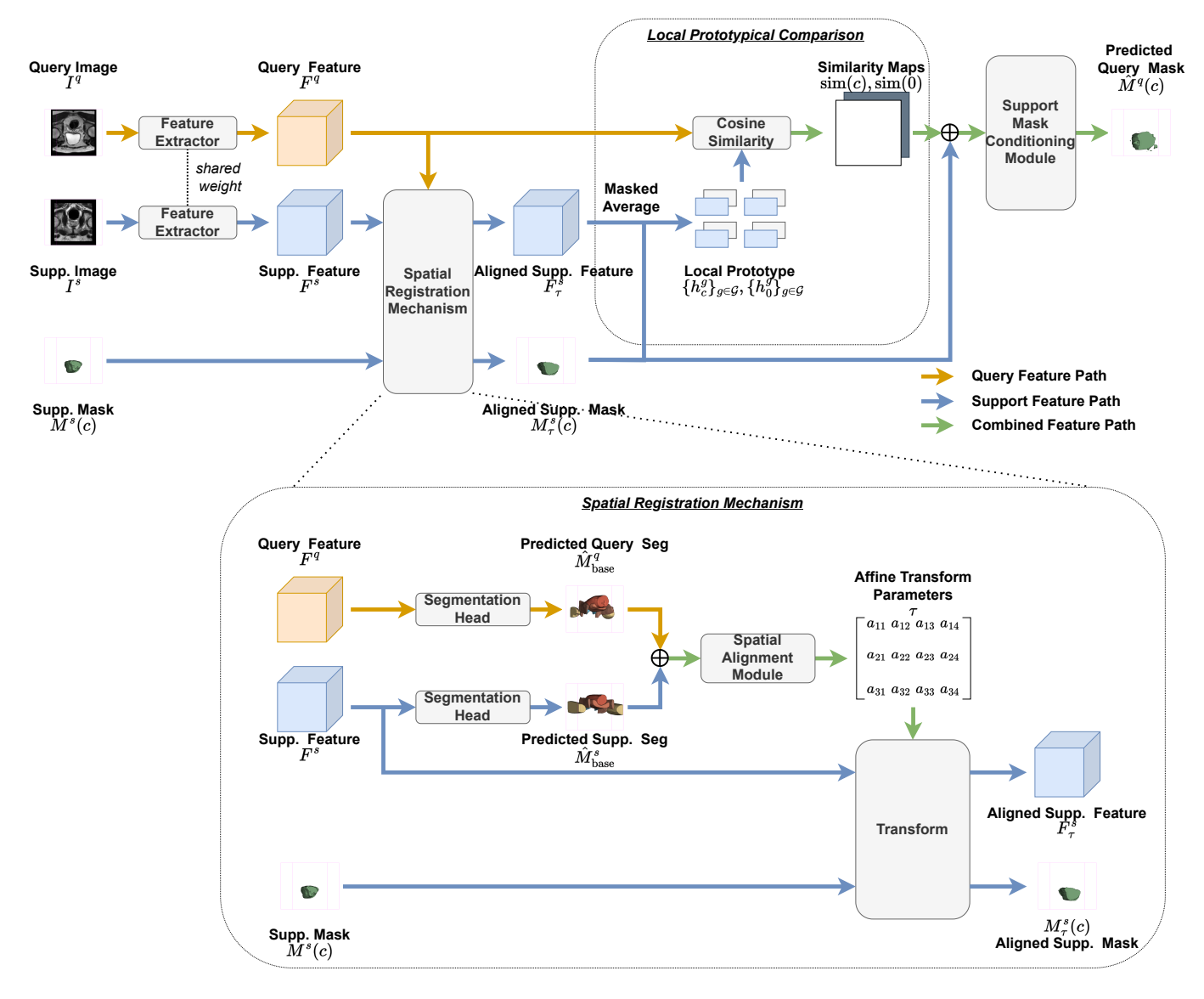


Fig. 2. Overview of the proposed method. A shared feature extractor outputs query/support features from query/support images. The spatial registration mechanism spatially registers support feature/mask towards query. Foreground/background similarity maps are derived through local prototypical comparison, concatenated with the aligned support mask and processed by the support mask conditioning module to make the final prediction

## 4. Method

## 4.1. Episodic Few-shot Training

This work adopts the common episodic training paradigm (detailed in Algorithm 2) that simulates the few-shot task during training. Each *episode* consists of query  $(I^q, M(I^q, c))$  and K support  $\{(I_k^s, M(I_k^s, c))\}_{k=1}^K$  image-label pairs, for a base class c sampled from  $C_{\text{base}}$ . In this work, K=1 during training and the model is trained to predict the query mask  $M^q(c)$  given the query image  $I^q$  and one support image-label pair, denoted as  $(I^s, M^s(c))$ .

## 4.2. Prototypical Network

A prototypical network (Dong and Xing, 2018) first defines a prototype feature vector per class, extracted from the embedded features of the labelled voxels, in the support image, corresponding to the class. The feature vector is then compared with

## **Algorithm 2:** Episodic Training Procedure

input: Neural network  $\phi_{\theta}$  with parameters  $\theta$ .

Learning rate  $\alpha$ .

Images  $I_u^{\text{train}}$  for all base institutions  $u \in \mathcal{U}_{base}$ .

Masks for all base classes in  $C_{\text{base}}$ .

output: Trained model  $\phi_{\theta}$ .

while Training do

Sample  $c \sim C_{base}$ Sample  $I^q$ ,  $I^s \in \bigcup_{u \in \mathcal{U}_{base}} I_u^{\text{train}}$ , such that  $I_s \neq I_q$ Denote the mask of c in  $I^s$  as  $M^s(c)$ Denote the mask of c in  $I^q$  as  $M^q(c)$ Predict  $\hat{M}^q(c) = \phi_{\theta}(I^q, I^s, M^s(c))$ 

Compute loss: *L* 

Update model parameters:  $\theta = \theta - \alpha \nabla_{\theta} L$ 

end

the query image voxel-wise in the embedded feature space for segmentation prediction.

Specifically, the query and support images, denoted by  $I^s$  and  $I^q$  respectively, are encoded by a shared feature extractor into support and query feature maps of the same shape,  $F^s$  and  $F^q$ , respectively. The class prototype  $h_c$  and the background prototype  $h_0$  are then derived by averaging  $F^s$  over voxels of the class c (where label  $M^s(c)$  equals 1) and background (where label  $M^s(c)$  equals 0), respectively, i.e.,  $h_c = f(F^s, M^s(c))$  and  $h_0 = f(F^s, 1 - M^s(c))$ , where

$$f(F,M) = \frac{\sum_{(x,y,z)} F_{(x,y,z)} M_{(x,y,z)}}{\sum_{(x,y,z)} M_{(x,y,z)}},$$
 (5)

with (x, y, z) iterating over all voxels in F along x, y and z axes. The similarity between each query voxel and class (or background) is calculated through cosine similarity between the voxel feature map  $F^q$  and the class prototype feature vector  $h_c$  (or  $h_0$  for background):

$$sim(\star) = \frac{F_{(x,y,z)}^{q} \cdot h_{\star}}{\|F_{(x,y,z)}^{q}\|_{2} \|h_{\star}\|_{2}},$$
(6)

where  $\star \in \{c, 0\}$  represents the class or background, and  $\cdot$  represents the dot product between vectors.

## 4.3. Local Prototypical Network

To extract location-sensitive local prototypes (Yu et al., 2021), images of spatial size  $W \times H \times D$  are partitioned into overlapping windows  $g \in G$  of size  $\alpha_w W \times \alpha_h H \times \alpha_d D$  with the equidistant spacing between window centres being half of the window size. As shown in Fig. 2, for each window  $g \in G$ , two local prototype feature vectors  $h_c^g$  and  $h_0^g$  are calculated via Eq. (5) by iterating (x, y, z) over the voxels inside the window  $g \colon h_c^g = f(F^s, M^s(c), g)$  and  $h_0^g = f(F^s, 1 - M^s(c), g)$ , where

$$f(F, M, g) = \frac{\sum_{(x, y, z) \in g} F_{(x, y, z)} M_{(x, y, z)}}{\sum_{(x, y, z) \in g} M_{(x, y, z)}}.$$
 (7)

For each query voxel (x, y, z),  $\mathcal{G}_{(x,y,z)}$  denotes the set of all windows that contains the voxel:  $\mathcal{G}_{(x,y,z)} = \{g \mid (x,y,z) \in g\}$ . The local similarity between this voxel and the class (or background) is then calculated using the maximum cosine similarity over windows  $g \in \mathcal{G}_{(x,y,z)}$  with the corresponding local prototype feature vectors  $\{h_c^g\}_{g \in \mathcal{G}_{(x,y,z)}}$  and  $\{h_0^g\}_{g \in \mathcal{G}_{(x,y,z)}}$ :

$$sim(\star) = \max_{g \in \mathcal{G}_{(x,y,z)}} \frac{F_{(x,y,z)}^q \cdot h_{\star}^g}{\|F_{(x,y,z)}^q\|_2 \|h_{\star}^g\|_2}$$
(8)

with  $\star \in \{c, 0\}$  representing the class or background. The foreground/background probability map is derived by:

$$\hat{M}^{q}(\star) = \frac{\exp(\operatorname{sim}(\star))}{\exp(\operatorname{sim}(0)) + \exp(\operatorname{sim}(c))} \tag{9}$$

with  $\star \in \{c, 0\}$  representing the class and background. The model is trained to minimise the Dice loss between the predicted and ground-truth mask:

$$L_{\text{fewshot}} = 1 - \sum_{\star \in \{0,c\}} \frac{2 \sum_{(x,y,z)} \hat{M}^q(\star)_{(x,y,z)} M^q(\star)_{(x,y,z)}}{\sum_{(x,y,z)} \hat{M}^q(\star)_{(x,y,z)}^2 + \sum_{(x,y,z)} M^q(\star)_{(x,y,z)}^2}$$
(10

where  $M^{q}(0) = 1 - M^{q}(c)$ 

## 4.4. Spatial Registration Mechanism

As discussed in Section 1, the differences in intra- and interinstitution variations pose challenges in the local prototypical network due to the varying image sizes, orientations, and voxel dimensions of the acquiring institution. The target structure in the query and support images can be distant (as in Fig. 10). Therefore, they may not be included inside of the same or even adjacent windows, and this results in erroneous comparison between the query voxels of the structure, thus irrelevant prototype vectors. However, while the absolute locations of target structures varies among images, the relative position between different structures remains consistent. This observation motivated spatial alignment of the query and the support images,  $I^q$ and  $I^s$ , illustrated in Fig. 2, before extracting the local prototype feature vectors. This spatial registration process is conjectured to alleviate the discrepancy between different institutions and therefore reduce the amount of cross-institution training data required for generalisation.

In this work, we consider an affine transformation to account for the above-discussed spatial difference with potentially uncertainties due to variable imaging positioning, signal sampling and scanner calibration, although higher-degree transformation will also be of interest. Furthermore, to avoid repeated feature map extraction, we propose to apply the transformation directly on feature maps ( $F^q$  and  $F^s$ ), rather than on images ( $I^q$  and  $I^s$ ).

The affine transformation prediction consists of two stages. Firstly, a shared base class segmentation head segments all base classes from the query and support feature maps,  $F^q$  and  $F^s$ , respectively. The multi-class predictions are denoted as  $\hat{M}_{\text{base}}^q$  and  $\hat{M}_{\text{base}}^s$ , for the query and support images, respectively. During evaluation, these predictions are concatenated and passed into the *spatial alignment module*, illustrated in Fig. 2, which predicts an affine transformation matrix  $\tau \in \mathbb{R}^{3\times 4}$  of 12 degrees of freedom. During training, as illustrated in Fig. 3, base classes segmentation masks  $M_{\text{base}}^q$  and  $M_{\text{base}}^s$  are used for alignment prediction. Secondly, alignment  $\tau$  is applied to the support feature map  $F^s$  and the label  $M_{\text{base}}^s$ , to obtain the aligned support feature map  $F_{\tau}^s = \tau \circ F^s$  and the aligned support label for all base classes  $M_{\tau,\text{base}}^s = \tau \circ M_{\text{base}}^s$ , respectively. These aligned feature maps are then used to generate the local prototypes (as detailed in Section 4.3) for segmentation.

Two losses are defined for training the spatial registration mechanism. First, a Dice loss is defined for the multi-class segmentation:

$$L_{\text{base seg}} = L_{\text{multi-class}}(\hat{M}_{\text{base}}^q, M_{\text{base}}^q) + L_{\text{multi-class}}(\hat{M}_{\text{base}}^s, M_{\text{base}}^s), \tag{11}$$

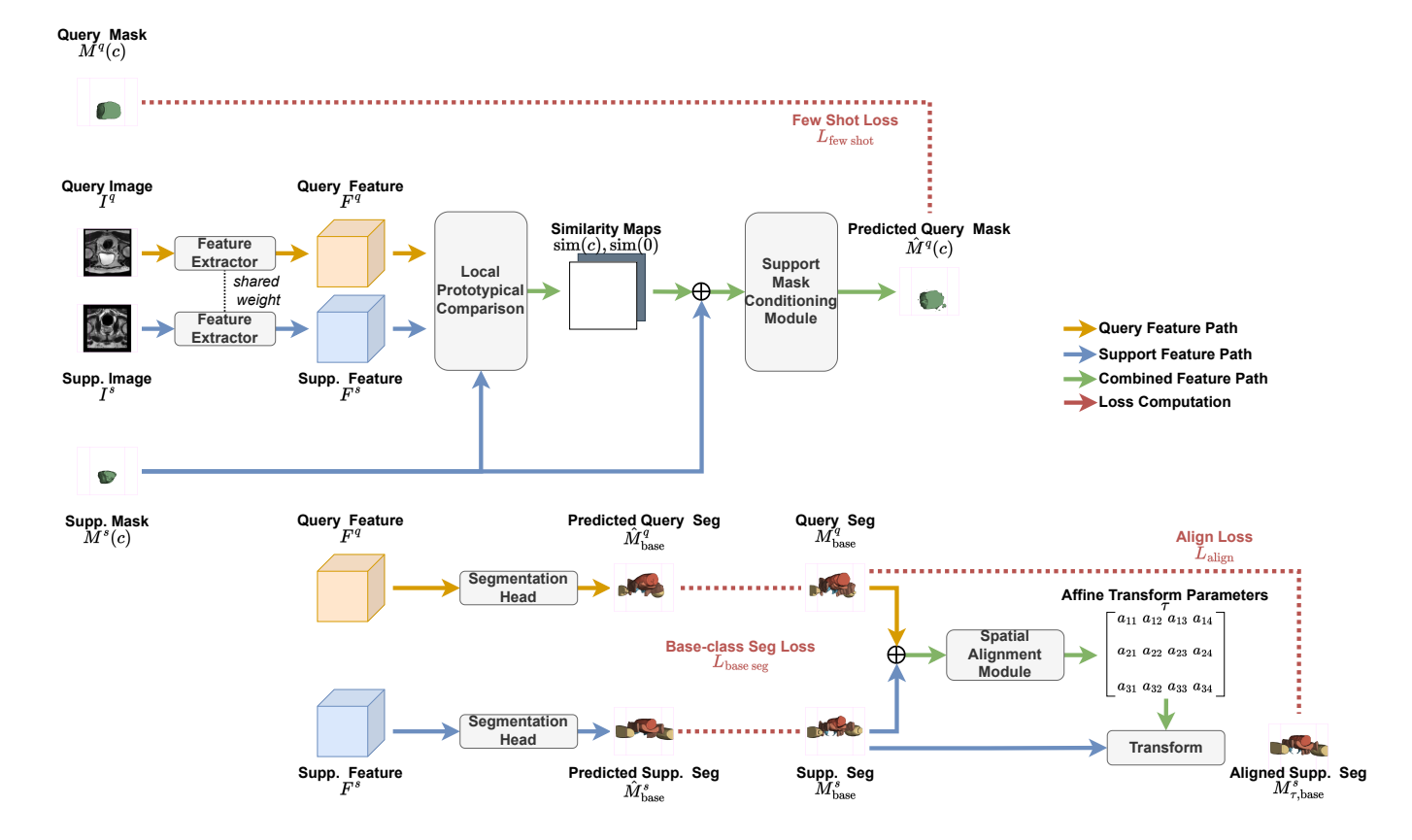


Fig. 3. The training procedure of the proposed method. The model is trained to minimise the sum of few-shot loss (Eq. 10), base class segmentation loss (Eq. 11) and alignment loss (Eq. 13).

where the multi-class Dice loss is defined as:

$$L_{\text{multi-class}}(M, \hat{M})$$

$$=1 - \sum_{\star \in C_{\text{base}} \cup \{0\}} \frac{2 \sum_{(x, y, z)} \hat{M}(\star)_{(x, y, z)} M(\star)_{(x, y, z)}}{\sum_{(x, y, z)} \hat{M}(\star)_{(x, y, z)}^2 + \sum_{(x, y, z)} M(\star)_{(x, y, z)}^2}$$
(12)

with  $M(\star)_{(x,y,z)}$  and  $\hat{M}(\star)_{(x,y,z)}$  representing the ground truth and the predicted probability of a base class or background  $\star$  at (x,y,z).

The second loss aims to optimise alignment by minimising the Dice loss between the query label  $M_{\rm base}^q$  and the aligned support label  $M_{\rm thase}^s$  of all base classes:

$$L_{\text{align}} = L_{\text{multi-class}}(M_{\text{base}}^q, M_{\tau, \text{base}}^s). \tag{13}$$

## 4.5. Support Mask Conditioning Module

During the prototype feature vector extraction using the novel class mask in the support image, the voxel-wise information may be made invariant to the transformation during the aggregation in Eq. (5) and (7), which is designed for "normalising" cross-institution data, but may also result in large spatial variability in the prediction. Therefore, a simple yet effective support mask conditioning module is proposed.

The support mask conditioning module takes as input a concatenation of the class similarity sim(c), the background similarity sim(0) and the aligned mask of the class in the support

image  $M_{\tau}^{s}(c)$ , for the final prediction  $\hat{M}^{q}(c)$ . Unlike the multiplication of support mask to support features for prototype calculation (in Eq. (5) and (7)), the direct use of support mask here provides a more direct route for the novel class information to the final segmentation task, similar to commonly designed shortcut layers for skipping networks.

## 4.6. Loss

Both the spatial registration mechanism and support mask conditioning module are trained with the original local prototypical network, with an overall training loss function used in this study as follows:

$$L = L_{\text{fewshot}} + L_{\text{base seg}} + L_{\text{align}}$$
 (14)

## 4.7. Multiple-shot Evaluation

Due to memory limitation, the training was carried out in one-shot paradigm, i.e. K=1. During the evaluation, for the query image  $I^q$  and each of the K support images  $I^s_k$ , the base class segmentation is predicted from the base class segmentation head, denoted by  $\hat{M}^q_{\text{base}}$  and  $\hat{M}^s_{\text{base},k}$ , respectively. Among the K support images, only the support image that is the most similar to the query image in terms of the cosine similarity on base class segmentation prediction, denoted by  $I^s_k$ , is chosen to calculate the local prototypes in (7). Precisely,

$$\hat{k} = \arg\max_{k} \frac{\hat{M}_{\text{base},k}^{s} \cdot \hat{M}_{\text{base}}^{q}}{\|\hat{M}_{\text{base},k}^{s}\|_{2} \|\hat{M}_{\text{base}}^{q}\|_{2}},$$
(15)

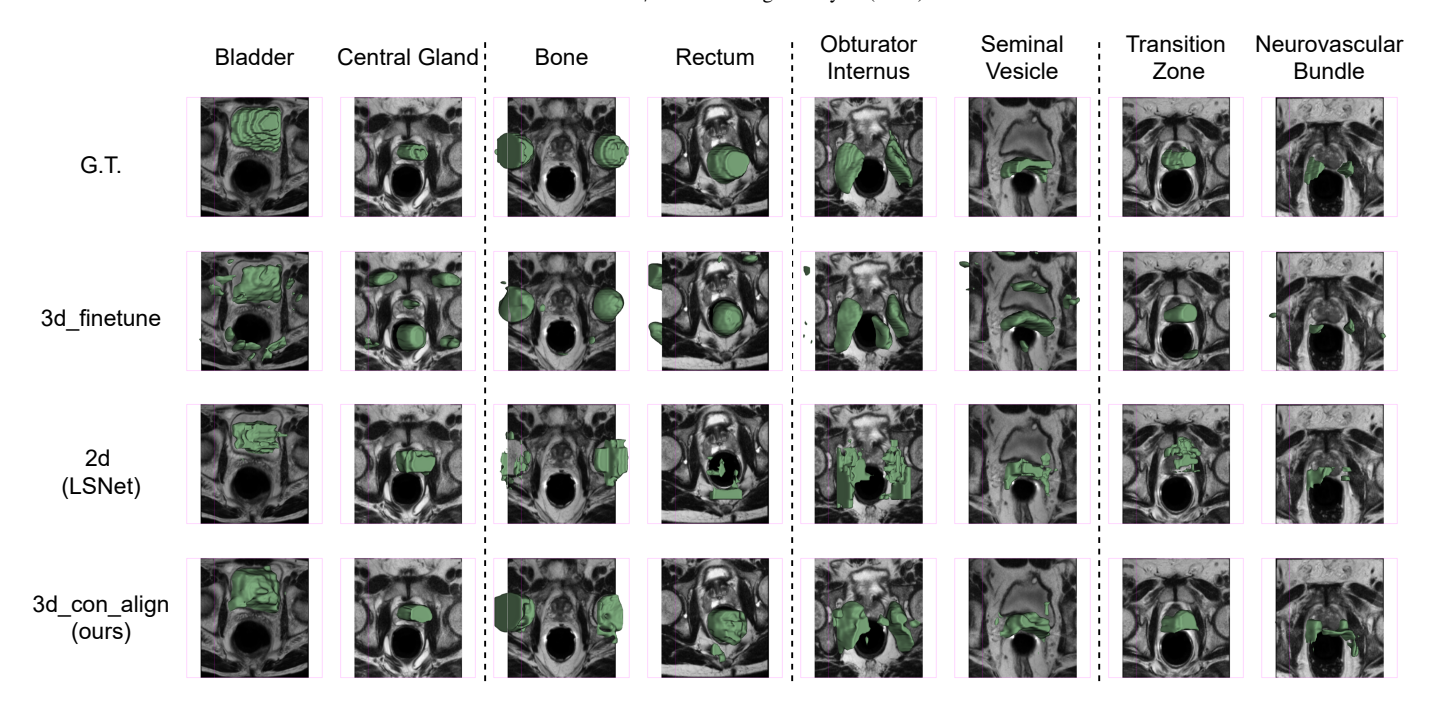


Fig. 4. Qualitative result achieved by '3d\_finetune' and '2d' baselines (detailed in Section 5.3) and our proposed method.

Table 1. The number of images acquired from each institution.

		institution									
	1	2	3	4	5	6	7	total			
# of images	296	45	74	82	25	25	25	589			

where the dot product and norm are calculated on the flattened predictions. The local prototypes are then calculated using the selected support example,  $h_c^g = f(F_{\hat{k}}^s, M(I_{\hat{k}}^s, c), g)$  and  $h_0^g = f(F_{\hat{k}}^s, 1 - M(I_{\hat{k}}^s, c), g)$  for each window g.

## 5. Experiments

## 5.1. Data Set

The data set includes 589 T2-weighted images acquired from the same number of patients collected by seven studies, INDEX (Dickinson et al., 2013), the SmartTarget Biopsy Trial (Hamid et al., 2019), PICTURE (Simmons et al., 2014), TCIA Prostate3T (Litjens et al., 2015), Promise12 (Litjens et al., 2014), TCIA ProstateDx (Diagnosis) (Bloch et al., 2015) and the Prostate MR Image Database (Choyke et al., 2016). Further details are reported in the respective study references.

These images were divided into seven subsets based on the acquiring institution. The number of images acquired from each institution is anonymously summarised in Table 1. The cross-institution imaging protocols contain multiple scanners (two manufacturers with a mixed 1.5 and 3T field strengths), varying field-of-view and anisotropic voxels, in-plane voxel dimensions ranging between 0.3 and 1.0 mm and out-of-plane spacing between 1.8 and 5.4 mm.

For each image, eight anatomical structures of planning interest, including bladder, bone, central gland, neurovascular bundle, obturator internus, rectum, seminal vesicle, transition zone

Table 2. The eight structures are randomly divided into 4 folds.

	g
	structures
fold 1	bladder, central gland
fold 2	bone, rectum
fold 3	obturator internus, seminal vesicle
fold 4	transition zone, neurovascular bundle

were labelled (as shown in Fig.4). All segmentations were manually annotated by eight biomedical imaging researchers, with experience ranging from 2 to 10 years in the annotation of medical image data, each annotating a mixed-institution subset using an institution-stratified sampling. Each annotation has been reviewed at least once.

The full segmentation masks and the derived intensity arrays from T2-weighted sequences, after pre-processing, used to produce the results in this study, are available at https://zenodo.org/record/7013610.

The eight lower-pelvic structures were randomly divided into four folds as shown in Table 2. In a cross-validation experiment, the classes contained in each fold were considered as novel classes, the other three folds representing base classes. The images of each institution u were then randomly sampled into training and testing subsets in a 3:1 ratio. A further validation set was formed with 12 images, 2 from each institution, randomly chosen from the novel data set  $\mathcal{D}_{novel}$ . Those images were excluded from the testing. Unless otherwise specified, the same data partitioning was used for all the results presented. All statistical conclusions are reported using paired Student's t-tests at the significance level of  $\alpha_{t-test} = 0.05$ .

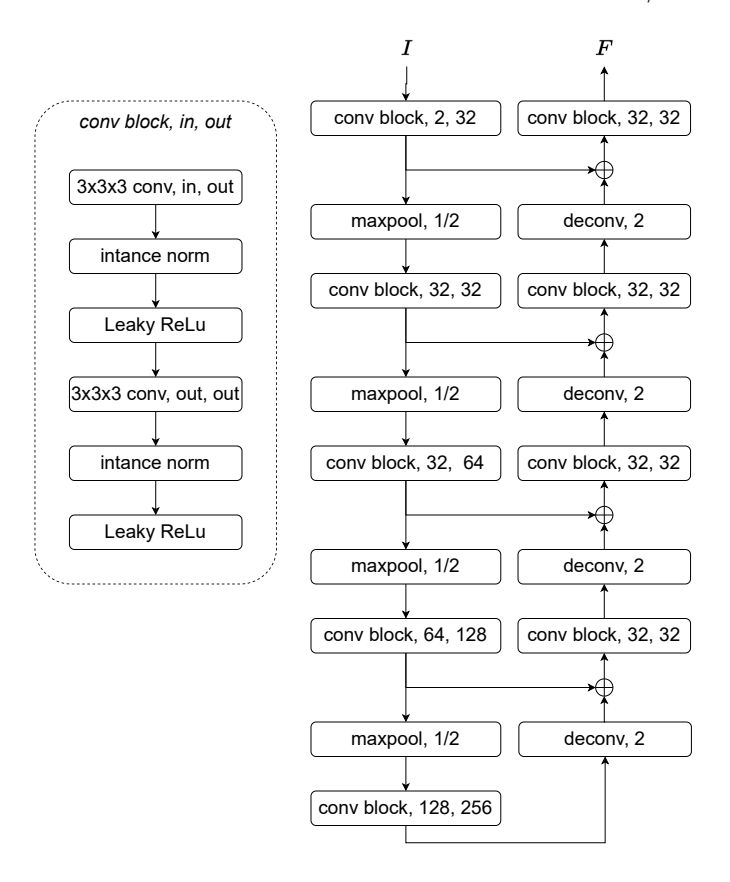


Fig. 5. Feature extractor architecture.

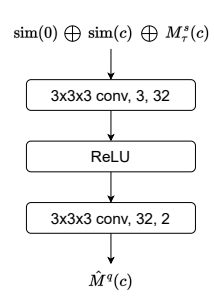


Fig. 6. Support mask conditioning module architecture.

## 5.2. Implementation Details

All images were normalised, resampled and centre-cropped to an image size of  $256 \times 256 \times 48$ , with a voxel dimension of  $0.75 \times 0.75 \times 2.5$  during pre-processing. Random rotation, translation and scaling were adopted for data augmentation during training.

The best training episode was chosen based on the performance on the validation sets. During evaluation, all images from the novel institution were considered query images for evaluation for each of the fold-specified novel classes. A binary Dice score for this novel class was calculated for each query image based on a sampled support image from each of the seven institutions, excluding the query. As described in Algorithm 1, the results were reported when support images from 1) all institutions, 2) base institutions, and 3) novel institutions. The institution where the support image comes from is denoted as

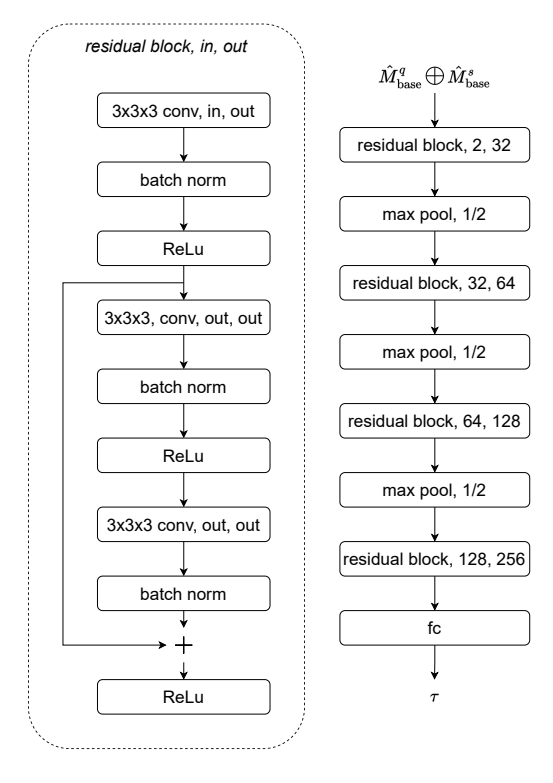


Fig. 7. Spatial alignment module architecture.

's\_ins'.

A 3D UNet was adopted as the feature extractor, whose architecture is detailed in Fig. 5.  $\alpha_w = \alpha_h = \frac{1}{8}$  and  $\alpha_d = 1$  were selected for local prototypical comparison as detailed in Section 4.3. As shown in Fig. 6, the support mask conditioning module was made up of two convolutional layers. For the spatial registration mechanism, the base class segmentation head was a single convolutional layer, and the spatial alignment module was a GlobalNet (Hu et al., 2018) as specified in Fig. 7. The models were trained using an Adam optimiser starting at a learning rate of  $10^{-4}$  with a minibatch size of 1. The implementation code has been released at https://github.com/kate-sann5100/CrossInstitutionFewShotSegmentation.

## 5.3. Compared Baseline Networks

For comparison, we report the results of the following baseline networks.

- 1. The '3d\_finetune' network The '3d\_finetune' baseline implemented the same UNet as the feature extractor. It was pre-trained on the base data set to segment all base classes for 100 epochs using an Adam optimiser starting at a learning rate of 10<sup>-4</sup>. During evaluation, for each query, the pre-trained model is fine-tuned on the support images for 10 iterations before testing. This baseline provides a reference as a "lower-bound" performance, using a simple transfer learning strategy.
- The '2d' network LSNet (Yu et al., 2021) was adopted as the 2D episodic baseline. It adopted the same localprototype comparison approach as detailed in Section 4.3 but using a 2D backbone based on ResNet-50 pre-trained

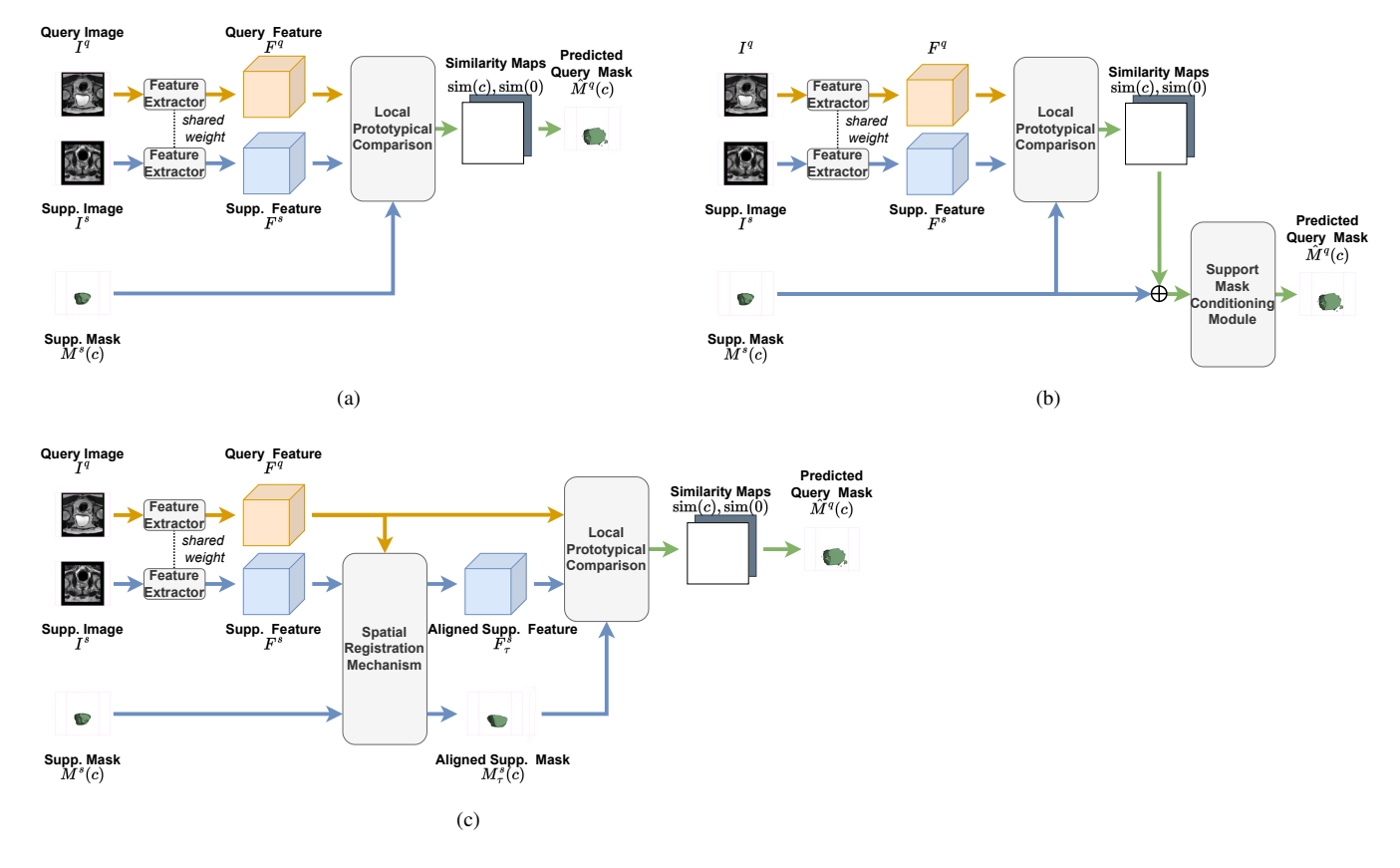


Fig. 8. Illustration of the three model variations (a) '3d' (b) '3d\_con' (c) '3d\_align' experimented for ablation studies (Section 5.4)

on ImageNet, instead of 3D networks. To the best of our knowledge, this is the prototypical network closest to our work that has been proposed for medical image segmentation.

3. The '3d\_supervised' network - A fully supervised 3D model was trained on the base data set images with masks from all classes. The results on the novel institution images are reported as an "upper-bound" performance.

## 5.4. Ablation Studies

**Ablation on different modules** To assess the effectiveness of different modules in the proposed method, we report the results of the following variations.

- 1. The '3d' network variant The proposed 3D local prototypical network, detailed in Section 4.3 and Fig. 8(a), without the support mask conditioning or spatial registration.
- 2. The '3d\_con' network variant The '3d' version with the support mask conditioning, but without the spatial registration, described in Section 4.5 and Fig. 8(b)).
- 3. The '3d\_align' network The '3d' version of the proposed network (detailed in 8(c)) with the spatial registration mechanism, without the support mask conditioning.
- 4. The '3d\_con\_align' network The "complete" version of the proposed network with both the support mask conditioning module and the spatial registration mechanism, as shown in Fig. 2.

**Ablation study on the number of shots** We report model performance when different number of support trios available in each episode.

Ablation on varying training data availability To investigate the dependency of our proposed method on the training set, we report the performance of the proposed model (3d\_con\_align) trained on various availability in training sets. The 'half' and 'quarter' experiments respectively includes  $\frac{1}{2}$  and  $\frac{1}{4}$  of the training subset  $\mathcal{D}_u^{train}$  for each base institutions  $u \in \mathcal{U}_{base}$ , in order to test the impact of the training data set size on the few-shot segmentation performance. The same ratio between institutions was maintained in these experiments. Additionally, the 'half\_single\_ins' experiment tests the same number of images as the 'half' experiment, but all the images are sampled from the same institution (Institution 1).

To assess and compare the intra- and inter-institution generlisation, results are also reported when all the institutions, only the base institutions and only the novel institutions were used as support institutions, denoted as 'all', 'base' and 'novel', respectively.

## 6. Results

The Dice score and 95% Hausdorff distance achieved by variations of our proposed method as well as the baseline networks are presented for comparison. Table 3 and 4 summarise the network performances, with respect to different folds and the

Table 3. Dice score (%) and 95% Hausdorff distance achieved when institution 3 was adopted as the novel institution. s\_ins refers to the institution from which the support images were sampled from.  $\Delta$  refers to the percentage difference between predictions made with support images from the base and novel institutions.

				D: (01)			95% Hausdorff distance (mm)						
model	s_ins			Dice (%)									
		fold1	fold2	fold3	fold4	mean	fold1	fold2	fold3	fold4	mean		
	all	48.07	44.78	43.92	29.25	41.50	61.47	69.78	60.33	57.02	62.15		
3d_finetune	base	45.74	39.81	41.69	26.02	38.32	63.22	73.42	62.33	59.24	64.55		
3d_inictuite	novel	62.03	74.56	57.31	48.63	60.63	50.98	47.96	48.32	43.72	47.74		
	Δ	26.26%	46.60%	27.25%	46.48%	36.80%	-24.02%	-53.09%	-28.99%	-35.51%	-35.21%		
	all	49.23	44.51	36.34	27.44	39.38	24.03	30.86	29.51	30.77	28.79		
2d	base	48.80	42.92	35.52	26.83	38.52	24.12	31.93	30.30	31.54	29.47		
20	novel	51.80	54.07	41.28	31.08	44.56	23.52	24.39	24.83	26.13	24.72		
	Δ	5.80%	20.62%	13.94%	13.68%	13.55%	-2.54%	-30.92%	-22.03%	-20.72%	-19.24%		
	all	47.79	52.06	34.81	26.16	40.20	31.60	30.68	32.95	31.71	31.73		
3d	base	47.89	51.07	34.12	25.44	39.63	31.69	31.03	33.35	32.19	32.07		
30	novel	47.22	58.00	38.96	30.49	43.67	31.07	28.54	30.54	28.81	29.74		
	Δ	-1.42%	11.94%	12.44%	16.58%	9.25%	-2.00%	-8.73%	-9.20%	-11.73%	-7.82%		
	all	58.34	46.11	40.43	30.94	43.96	27.31	27.15	27.33	26.38	27.04		
3d_con	base	58.25	43.58	39.87	29.80	42.88	27.69	28.34	28.03	27.06	27.78		
Su_con	novel	58.84	61.30	43.81	37.78	50.43	25.04	20.02	23.14	22.30	22.63		
	Δ	1.00%	28.91%	8.99%	21.12%	14.98%	-10.56%	-41.54%	-21.12%	-21.31%	-22.76%		
	all	50.80	51.56	32.39	30.89	41.41	27.33	36.29	32.63	29.93	31.55		
2d alian	base	50.60	51.17	31.25	30.82	40.96	27.35	36.82	33.01	30.42	31.90		
3d_align	novel	51.97	53.88	39.22	31.33	44.10	27.20	33.15	30.34	26.96	29.41		
	Δ	2.64%	5.04%	20.31%	1.62%	7.12%	-0.55%	-11.08%	-8.78%	-12.84%	-8.46%		
	all	59.36	60.38	45.73	37.60	50.77	22.66	29.63	27.92	26.41	26.66		
2.11:	base	59.11	59.80	45.06	37.28	50.31	22.69	30.30	28.38	26.89	27.06		
3d_con_align	novel	60.86	63.87	49.77	39.54	53.51	22.49	25.63	25.19	23.54	24.21		
	Δ	2.89%	6.37%	9.47%	5.70%	5.98%	-0.91%	-18.21%	-12.65%	-14.26%	-11.79%		
3d_supervised	N/A	89.01	91.68	81.44	70.30	83.11	4.73	5.14	5.91	6.83	5.65		

Table 4. Dice score (%) and 95% Hausdorff distance achieved when institution 4 was adopted as the novel institution. s\_ins refers to the institution from which the support images were sampled from.  $\Delta$  refers to the percentage difference between predictions made with support images from the base and novel institutions.

model	a inc			Dice (%)				95% Haus	dorff dista	nce (mm)	
model	s_ins	fold1	fold2	fold3	fold4	mean	fold1	fold2	fold3	fold4	mean
	all	37.61	29.23	33.06	20.25	30.04	59.83	71.87	50.66	51.62	58.49
3d_finetune	base	36.72	28.33	31.11	20.02	29.05	60.77	73.85	52.09	52.02	59.68
3d_IIIIetulie	novel	42.96	34.63	44.73	21.63	35.99	54.16	59.97	42.09	49.20	51.36
	Δ	14.53%	18.17%	30.45%	7.43%	19.29%	-12.21%	-23.13%	-23.75%	-5.74%	-16.22%
	all	42.09	29.00	32.49	24.46	32.01	29.52	42.65	28.04	31.97	33.05
2d	base	41.83	28.51	32.09	24.47	31.73	29.62	42.39	28.08	31.93	33.01
20	novel	43.64	31.92	34.85	24.41	33.71	28.90	44.18	27.80	32.19	33.27
	Δ	4.14%	10.68%	7.92%	-0.26%	5.87%	-2.50%	4.05%	-1.00%	0.80%	0.79%
	all	57.58	37.42	37.42	30.18	40.65	23.02	37.56	30.22	28.52	29.83
3d_con_align	base	57.71	36.74	36.70	29.97	40.28	22.90	38.37	30.74	28.52	30.13
3u_con_angn	novel	56.83	41.46	41.70	31.40	42.85	23.75	32.72	27.12	28.51	28.02
	Δ	-1.54%	11.39%	11.99%	4.56%	6.00%	3.58%	-17.26%	-13.36%	-0.04%	-7.52%
3d_supervised	N/A	88.31	88.44	80.49	70.78	82.00	5.14	7.72	6.49	6.71	6.51

mean of all folds using institution 3 and 4 as the novel institution, respectively. Other institutions were not used as novel institution as they have either too many or too few samples such that the training or test set size will be too small. When institution 3 is used as the novel institution (Table 3), the proposed method with both support mask conditioning module and spatial registration mechanism ('3d\_con\_align') outperformed the '2d' baseline by 11.39%, 11.79% and 8.95% absolute Dice improvements, when support images came from all, base and novel institutions, respectively. While the '3d\_finetune' base-

line achieved higher Dice than the '2d' baseline, its 95% Hausdorff distance is more than double of the '2d' baseline. This could be related to the commonly appearing false positive predictions as shown in Fig. 4. Similar improvements have also been observed when Institution 4 was adopted as the novel institution. 8.64%, 8.55% and 9.15% absolute Dice improvements over the '2d' baseline were achieved by the proposed method, as support images came from all, base and novel institutions, respectively (Table 4). The relative difference between performances when support images come from base and novel institutions.

tutions, denoted as performance gap  $\Delta$ , are also summarised in Table 3 and Table 4. While achieving better performance overall, the proposed method reported smaller performance gap.

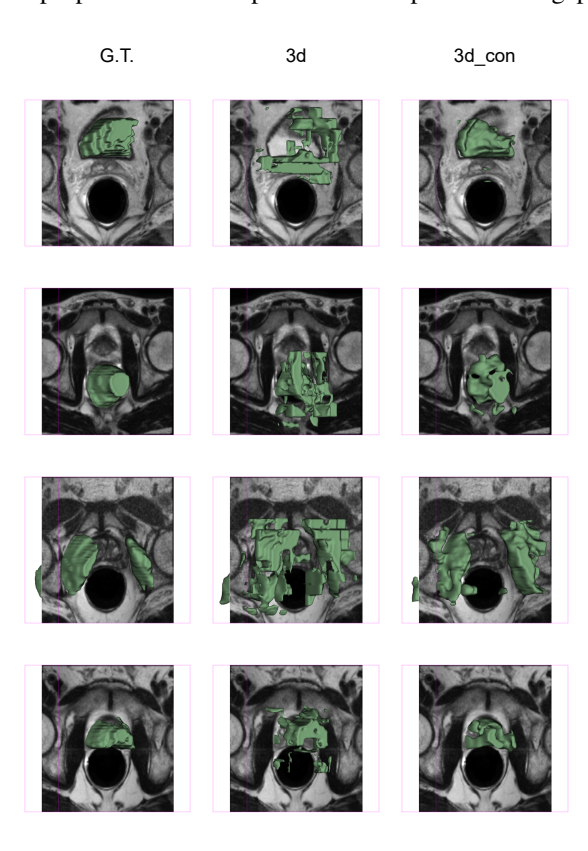


Fig. 9. Qualitative results achieved by '3d' and '3d\_con' on the same support-query pairs. '3d\_con' resulted in more compact segmentation with smoother boundary compare with '3d'

In particular, the support mask conditioning module provided an 3.76% absolute increase in Dice score comparing '3d\_con' to '3d'. Qualitatively, it also resulted in more "compact" segmentation with smoother boundary as shown in Fig. 9. However, it also resulted in a higher  $\Delta$ , possibly because of its sensitivity to support-query alignment.

This was mitigated by the spatial registration mechanism which not only further improved the Dice score by 6.81% but also reduced  $\Delta$  by 9.00%. Fig. 10 shows an example where the target structure of the query and support were misaligned, resulting in segmentation failure. Aligning the support towards query, the spatial registration mechanism considerably improved the performance.

It is also important to report that the proposed 3D network '3d' without the support mask conditioning module and the spatial registration mechanism contained 5.7 million parameters. It achieved comparable performance to the '2d' baseline with 23.5 million parameters, resulted in around 75% reduction in number of parameters. For reference, the complete version of our proposed method '3d\_con\_align' had contained 27.3 million parameters (16% more parameters compared with '2d'), had achieved 28.9% of relative Dice improvement over '2d'.

Furthermore, Table 5 and Table 6 report the mean Dice score achieved by '2d' and '3d\_con\_align' from different support-

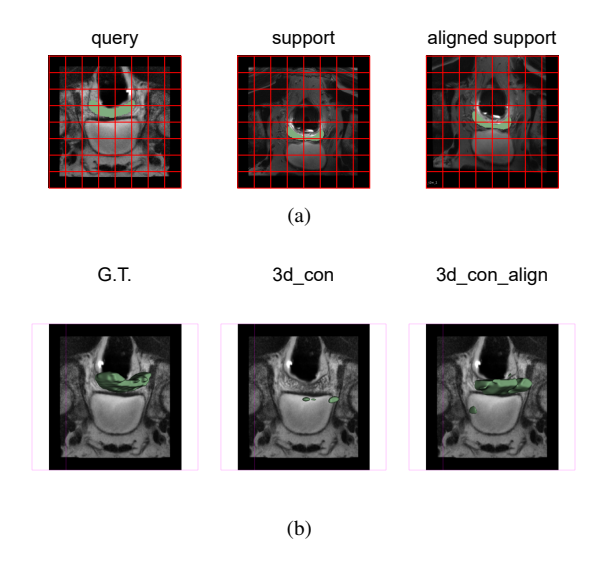


Fig. 10. Qualitative results achieved by '3d\_con' and '3d\_con\_align' on a misaligned query-support pair. (a) visualises the original query and support, as well as the support aligned towards query through the spatial registration mechanism. (b) visualises predictions made by '3d\_con' and '3d\_con\_align' based on the same support-query pair.

query institution combinations, when institution 3 is the novel institution. Better performance was often achieved by both methods when support images come from the query institution. A two tailed t-test is performed per query institution between the Dice scores where support institution equals query institution and the maximum Dice scores achieved when support institution differs from the query institution. Such observation is consistent with the hypothesis that the domain shift is smaller between support-query pairs within the same institution, leading to better performance.

Table 8. Dice score achieved by '3d\_con\_align' with various number of shots when Institution 3 was adopted as the novel institution. The s\_ins refers to the institution from which the support images were sampled from.

	VIII *** III	cii tiit su	pport in	iages were	Sumpice	110111					
# of shot	s_ins	Dice (%)									
# OI SHOU	8_1118	fold1	fold2	fold3	fold4	mean					
	all	59.36	60.38	45.73	37.60	50.77					
1	base	59.11	59.80	45.06	37.28	50.31					
1	novel	60.86	63.87	49.77	39.54	53.51					
	Δ	2.89%	6.37%	9.47%	5.70%	5.98%					
	all	60.64	60.41	47.82	38.91	51.95					
2	base	60.03	59.82	47.02	38.54	51.35					
	novel	64.28	63.94	52.66	41.12	55.50					
	Δ	6.61%	6.44%	10.71%	6.27%	7.47%					
	all	61.36	60.93	48.53	38.55	52.34					
3	base	61.06	60.27	47.99	38.25	51.89					
3	novel	63.13	64.88	51.80	40.33	55.03					
	Δ	3.28%	7.10%	7.35%	5.16%	5.71%					
	all	61.33	60.63	49.52	38.16	52.41					
4	base	60.69	59.91	49.01	37.56	51.79					
4	novel	64.52	64.23	52.08	41.19	55.50					
	Δ	5.94%	6.73%	5.90%	8.81%	6.69%					

Table 7 reports the performance achieved by the proposed method ('3d\_con\_align') as training set varies. The performance

Table 5. Mean Dice score (%) achieved at different (s.ins, q.ins) combinations by '2d' when Institution 3 was adopted as the novel institution, where s.ins and q.ins respectively refers to the institution from which the support and query were sampled from. Best performance for each query institution were bolded. p-values were derived from paired t-test performed between the Dice scores where support institution equals query institution and the maximum Dice scores achieved when support institution differs from the query institution.

					s_ins				std	mean	p-value
		ins1	ins2	ins3	ins4	ins5	ins6	ins7			
	ins1	48.41	44.67	39.78	33.23	43.89	42.28	29.84	6.11	40.30	8.14e-16
	ins2	46.42	49.15	37.66	27.39	42.35	43.05	29.09	7.74	39.30	5.38e-04
	ins3	41.60	38.36	44.56	37.14	40.34	37.30	36.37	2.73	39.38	1.62e-16
q_ins	ins4	34.39	32.12	35.46	39.00	31.11	29.77	35.28	2.89	33.88	0.71
	ins5	43.91	44.63	32.26	35.96	53.49	46.44	27.39	8.39	40.58	0.87
	ins6	41.83	44.59	39.03	29.64	46.39	44.33	30.79	6.27	39.51	4.51e-03
	ins7	32.75	30.87	33.62	35.53	28.12	24.28	34.52	3.69	31.38	0.09

Table 6. Mean Dice score (%) achieved at different (s\_ins, q\_ins) combinations by '3d\_con\_align' when Institution 3 was adopted as the novel institution, where s\_ins and q\_ins respectively refers to the institution from which the support and query were sampled from. Best performance for each query institution were bolded. p-values were derived from paired t-test performed between the Dice scores where support institution equals query institution and the maximum Dice scores achieved when support institution differs from the query institution.

					s_ins				std	mean	p-value
		ins1	ins2	ins3	ins4	ins5	ins6	ins7			
	ins1	53.76	53.31	50.63	46.46	50.77	47.78	47.83	2.62	50.08	1.06e-15
	ins2	54.26	57.74	50.07	44.42	51.97	52.05	48.62	3.91	51.30	0.08
	ins3	51.11	50.17	53.51	49.41	52.25	47.25	51.67	1.90	50.77	2.04e-16
q_ins	ins4	48.23	44.70	49.95	50.73	47.09	44.02	51.47	2.70	48.03	1.40e-05
	ins5	54.70	52.88	54.38	54.14	61.14	50.56	54.77	2.98	54.65	0.15
	ins6	52.10	55.89	51.69	44.23	52.70	52.02	51.61	3.26	51.46	9.47e-03
	ins7	46.46	45.81	48.77	48.78	45.45	41.57	49.85	2.60	46.67	0.20

Table 7. Dice score (%) and 95% Hausdorff distance achieved by '3d\_con\_align' with various training data availability when Institution 3 was adopted as the novel institution. s\_ins refers to the institution from which the support was sampled from.  $\Delta$  refers to the percentage difference when the support image comes from the base and novel institutions.

training Dice (%) 95% Hausdorff distance (mm)											
training	s_ins			Dice (%)	)			95% Hau	sdorff dist	ance (mm)	)
data	5_1115	fold1	fold2	fold3	fold4	mean	fold1	fold2	fold3	fold4	mean
	all	59.36	60.38	45.73	37.60	50.77	22.66	29.63	27.92	26.41	26.66
whole	base	59.11	59.80	45.06	37.28	50.31	22.69	30.30	28.38	26.89	27.06
WHOLE	novel	60.86	63.87	49.77	39.54	53.51	22.49	25.63	25.19	23.54	24.21
	Δ	2.89%	6.37%	9.47%	5.70%	5.98%	-0.91%	-18.21%	-12.65%	-14.26%	-11.79%
	all	55.38	57.16	42.54	34.14	47.30	25.98	29.37	31.65	29.00	29.00
half	base	55.08	55.49	41.82	33.75	46.54	26.04	30.13	32.17	29.37	29.43
IIaII	novel	57.16	67.17	46.88	36.46	51.91	25.56	24.81	28.52	26.84	26.43
	Δ	3.63%	17.38%	10.79%	7.41%	10.36%	-1.91%	-21.45%	-12.82%	-9.43%	-11.35%
	all	52.85	57.46	31.31	20.39	40.50	26.84	29.38	35.41	33.89	31.38
half_single_ins	base	52.17	56.06	30.55	19.63	39.60	26.93	29.93	36.04	34.41	31.83
man_single_ins	novel	56.90	65.87	35.85	24.93	45.89	26.29	26.10	31.65	30.75	28.70
	Δ	8.32%	14.89%	14.79%	21.24%	13.69%	-2.44%	-14.63%	-13.88%	-11.89%	-10.90%
	all	50.90	55.87	44.78	31.98	45.88	27.90	29.61	28.87	29.48	28.96
quarter	base	50.35	54.54	43.64	31.61	45.03	27.90	30.22	29.43	29.84	29.35
quarter	novel	54.24	63.86	51.61	34.17	50.97	27.88	25.92	25.50	27.27	26.64
	Δ	7.17%	14.60%	15.45%	7.49%	11.65%	-0.05%	-16.60%	-15.41%	-9.43%	-10.15%

dropped as the number of images inside the training set reduced. Notably, model trained on 'half\_single\_ins' performed worse than model trained on 'quarter', which had only half the size of 'half\_single\_ins'. This suggests that the cross-institution few-shot task can be sensitive to the number of institutions available in the training set. To quantify this sensitivity is an interesting future research question.

Regarding few-shot with more than one support images, the proposed method '3d\_con\_align' achieved incremental improvements as the number of support examples (denoted as #

shot) increases as shown in Table 8.

### 7. Discussion

While both the spatial registration mechanism and the support mask conditioning were motivated by the observation on multiple structure types found in the multi-institution data set used in this study, they may be promising to be beneficial for wider image types and anatomical regions as similar challenges were found in the few-shot segmentation of other types of nonmedical data.

The labels used in this study were annotated by a mixture of clinicians and experienced medical imaging researchers. The estimated time for completing this task was more than one thousand observer-hours, a practically challenging task for most local hospitals if an alternative supervised learning was adopted for adopting or validating a segmentation tool. This further justifies the clinical relevance for the proposed few-shot segmentation approach.

It is noteworthy that the reported segmentation performance results were based on as few as 1 - 4 labelled training examples of the regions of interest, which had not been labelled in the model training stage. Several questions remain subjects of future research include the achievability to fill the gap to the upper-bound performance from supervised learning, the clinical relevance of the reported accuracy and indeed the interpretation of Dice and 95% Hausdorff distance in different applications as a performance metric. However, They are considered first to report in this work for their intuitive definitions and for comparing with wider literature.

## 8. Conclusion

This paper described the first 3D prototypical learning algorithm for medical image segmentation, applied on multiple structures on pelvic MR images from different institutes. Substantial validation was based on clinical data from 589 patients, with full segmentation of eight anatomical classes made available to the scientific community. The demonstrated novelty, efficacy, and clinical applicability of the proposed algorithm suggested an interesting direction for addressing the cost of expert labelling and cross-institute generalisation of current deep learning-based segmentation applications.

## Acknowledgments

This work was supported by the International Alliance for Cancer Early Detection, a partnership between Cancer Research UK [C28070/A30912; C73666/A31378], Canary Center at Stanford University, the University of Cambridge, OHSU Knight Cancer Institute, University College London and the University of Manchester. This work was also supported by the Wellcome/EPSRC Centre for Interventional and Surgical Sciences [203145Z/16/Z], and EPSRC [EP/T029404/1, EP/S021930/1].

#### References

- Abdel-Basset, M., Chang, V., Hawash, H., Chakrabortty, R.K., Ryan, M., 2021. Fss-2019-ncov: A deep learning architecture for semi-supervised few-shot segmentation of covid-19 infection. Knowledge-Based Systems 212, 106647.
- Bloch, B.N., Jain, A., Jaffe, C.C., 2015. Data from prostate-diagnosis. The Cancer Imaging Archive doi:10.7937/K9/TCIA.2015.F0QEUJVT.
- Cho, K., Van Merriënboer, B., Bahdanau, D., Bengio, Y., 2014. On the properties of neural machine translation: Encoder-decoder approaches. arXiv preprint arXiv:1409.1259.

- Choyke, P., Turkbey, B., Pinto, P., Merino, M., Wood, B., 2016. Data from prostate-mri. The Cancer Imaging Archive doi:10.7937/K9/TCIA.2016. 6046GUDv.
- Cui, H., Wei, D., Ma, K., Gu, S., Zheng, Y., 2020. A unified framework for generalized low-shot medical image segmentation with scarce data. IEEE Transactions on Medical Imaging 40, 2656–2671.
- Dickinson, L., Ahmed, H.U., Kirkham, A., Allen, C., Freeman, A., Barber, J., Hindley, R.G., Leslie, T., Ogden, C., Persad, R., et al., 2013. A multicentre prospective development study evaluating focal therapy using high intensity focused ultrasound for localised prostate cancer: the index study. Contemporary clinical trials 36, 68–80.
- Dong, N., Xing, E.P., 2018. Few-shot semantic segmentation with prototype learning., in: BMVC.
- Feyjie, A.R., Azad, R., Pedersoli, M., Kauffman, C., Ayed, I.B., Dolz, J., 2020. Semi-supervised few-shot learning for medical image segmentation. arXiv preprint arXiv:2003.08462.
- Fiorino, C., Reni, M., Bolognesi, A., Cattaneo, G.M., Calandrino, R., 1998. Intra-and inter-observer variability in contouring prostate and seminal vesicles: implications for conformal treatment planning. Radiotherapy and oncology 47, 285–292.
- Fu, Y., Robu, M.R., Koo, B., Schneider, C., Laarhoven, S.v., Stoyanov, D., Davidson, B., Clarkson, M.J., Hu, Y., 2019. More unlabelled data or label more data? a study on semi-supervised laparoscopic image segmentation, in: Domain Adaptation and Representation Transfer and Medical Image Learning with Less Labels and Imperfect Data. Springer, pp. 173–180.
- Gibson, E., Hu, Y., Ghavami, N., et al., 2018. Inter-site variability in prostate segmentation accuracy using deep learning, in: International Conference on Medical Image Computing and Computer-Assisted Intervention, Springer. pp. 506–514.
- Guo, S., Xu, L., Feng, C., Xiong, H., Gao, Z., Zhang, H., 2021. Multi-level semantic adaptation for few-shot segmentation on cardiac image sequences. Medical Image Analysis 73, 102170.
- Hamid, S., Donaldson, I.A., Hu, Y., et al., 2019. The smarttarget biopsy trial: a prospective, within-person randomised, blinded trial comparing the accuracy of visual-registration and magnetic resonance imaging/ultrasound image-fusion targeted biopsies for prostate cancer risk stratification. European urology 75, 733–740.
- Han, X., Fischl, B., 2007. Atlas renormalization for improved brain mr image segmentation across scanner platforms. IEEE transactions on medical imaging 26, 479–486.
- He, Y., Li, T., Yang, G., Kong, Y., Chen, Y., Shu, H., Coatrieux, J.L., Dillenseger, J.L., Li, S., 2020. Deep complementary joint model for complex scene registration and few-shot segmentation on medical images, in: European Conference on Computer Vision, Springer. pp. 770–786.
- Henschel, L., Conjeti, S., Estrada, S., Diers, K., Fischl, B., Reuter, M., 2020. Fastsurfer-a fast and accurate deep learning based neuroimaging pipeline. NeuroImage 219, 117012.
- Hosseini-Asl, E., Keynton, R., El-Baz, A., 2016. Alzheimer's disease diagnostics by adaptation of 3d convolutional network, in: 2016 IEEE international conference on image processing (ICIP), IEEE. pp. 126–130.
- Howe, R.D., Matsuoka, Y., 1999. Robotics for surgery. Annual review of biomedical engineering 1, 211–240.
- Hu, Y., Modat, M., Gibson, E., Ghavami, N., Bonmati, E., Moore, C.M., Emberton, M., Noble, J.A., Barratt, D.C., Vercauteren, T., 2018. Label-driven weakly-supervised learning for multimodal deformable image registration, in: 2018 IEEE 15th International Symposium on Biomedical Imaging (ISBI 2018), IEEE. pp. 1070–1074.
- Hutchinson, M., Raff, U., 2000. Structural changes of the substantia nigra in parkinson's disease as revealed by mr imaging. American journal of neuroradiology 21, 697–701.
- Kim, S., An, S., Chikontwe, P., Park, S.H., 2021. Bidirectional rnn-based few shot learning for 3d medical image segmentation, in: Proceedings of the AAAI Conference on Artificial Intelligence, pp. 1808–1816.
- Li, A., Wang, S., Li, W., Liu, S., Zhang, S., 2020. Predicting human mobility with federated learning, in: Proceedings of the 28th International Conference on Advances in Geographic Information Systems, pp. 441–444.
- Li, X., Jiang, M., Zhang, X., Kamp, M., Dou, Q., 2021a. Fedbn: Federated learning on non-iid features via local batch normalization. arXiv preprint arXiv:2102.07623.
- Li, Y., Data, G.W.P., Fu, Y., Hu, Y., Prisacariu, V.A., 2021b. Few-shot semantic segmentation with self-supervision from pseudo-classes. arXiv preprint arXiv:2110.11742.

- Li, Y., Fu, Y., Yang, Q., Min, Z., Yan, W., Huisman, H., Barratt, D., Prisacariu, V.A., Hu, Y., 2022. Few-shot image segmentation for cross-institution male pelvic organs using registration-assisted prototypical learning, in: 2022 IEEE 19th International Symposium on Biomedical Imaging (ISBI), IEEE. pp. 1–5.
- Litjens, G., Futterer, J., Huisman, H., 2015. Data from prostate-3t. The Cancer Imaging Archive doi:10.7937/K9/TCIA.2015.QJTV5IL5.
- Litjens, G., Toth, R., van de Ven, W., et al., 2014. Evaluation of prostate segmentation algorithms for mri: the promise12 challenge. Medical image analysis 18, 359–373.
- Liu, Y., Zhang, X., Zhang, S., He, X., 2020. Part-aware prototype network for few-shot semantic segmentation, in: European Conference on Computer Vision, Springer. pp. 142–158.
- Meyer, A., Mehrtash, A., Rak, M., Bashkanov, O., Langbein, B., Ziaei, A., Kibel, A.S., Tempany, C.M., Hansen, C., Tokuda, J., 2021. Domain adaptation for segmentation of critical structures for prostate cancer therapy. Scientific reports 11, 1–14.
- Mondal, A.K., Dolz, J., Desrosiers, C., 2018. Few-shot 3d multi-modal medical image segmentation using generative adversarial learning. arXiv preprint arXiv:1810.12241.
- Ouyang, C., Biffi, C., Chen, C., et al., 2020. Self-supervision with superpixels: Training few-shot medical image segmentation without annotation, in: European Conference on Computer Vision, Springer. pp. 762–780.
- Perone, C.S., Ballester, P., Barros, R.C., Cohen-Adad, J., 2019. Unsupervised domain adaptation for medical imaging segmentation with self-ensembling. NeuroImage 194, 1–11.
- Petrella, J.R., Coleman, R.E., Doraiswamy, P.M., 2003. Neuroimaging and early diagnosis of alzheimer disease: a look to the future. Radiology 226, 315–336.
- Ren, J., Hacihaliloglu, I., Singer, E.A., Foran, D.J., Qi, X., 2018. Adversarial domain adaptation for classification of prostate histopathology whole-slide images, in: International conference on medical image computing and computer-assisted intervention, Springer. pp. 201–209.
- Rieke, N., Hancox, J., Li, W., Milletari, F., Roth, H.R., Albarqouni, S., Bakas, S., Galtier, M.N., Landman, B.A., Maier-Hein, K., et al., 2020. The future of digital health with federated learning. NPJ digital medicine 3, 1–7.
- De la Rosette, J., Ahmed, H., Barentsz, J., Johansen, T.B., Brausi, M., Emberton, M., Frauscher, F., Greene, D., Harisinghani, M., Haustermans, K., et al., 2010. Focal therapy in prostate cancer—report from a consensus panel. Journal of Endourology 24, 775–780.
- Roy, A.G., Siddiqui, S., Pölsterl, S., et al., 2020. 'squeeze & excite'guided few-shot segmentation of volumetric images. Medical image analysis 59, 101587.
- Shaban, A., Bansal, S., Liu, Z., et al., 2017. One-shot learning for semantic segmentation. arXiv preprint arXiv:1709.03410.
- Simmons, L.A., Ahmed, H.U., Moore, C.M., Punwani, S., Freeman, A., Hu, Y., Barratt, D., Charman, S.C., Van der Meulen, J., Emberton, M., 2014. The picture study—prostate imaging (multi-parametric mri and prostate histoscanning<sup>TM</sup>) compared to transperineal ultrasound guided biopsy for significant prostate cancer risk evaluation. Contemporary clinical trials 37, 69–83.
- Snell, J., Swersky, K., Zemel, R., 2017. Prototypical networks for few-shot learning. Advances in neural information processing systems 30.
- Sudre, C.H., Li, W., Vercauteren, T., Ourselin, S., Jorge Cardoso, M., 2017. Generalised dice overlap as a deep learning loss function for highly unbalanced segmentations, in: Deep learning in medical image analysis and multimodal learning for clinical decision support. Springer, pp. 240–248.
- Sun, L., Li, C., Ding, X., Huang, Y., Chen, Z., Wang, G., Yu, Y., Paisley, J., 2022. Few-shot medical image segmentation using a global correlation network with discriminative embedding. Computers in biology and medicine 140, 105067.
- Sung, F., Yang, Y., Zhang, L., Xiang, T., Torr, P.H., Hospedales, T.M., 2018. Learning to compare: Relation network for few-shot learning, in: Proceedings of the IEEE conference on computer vision and pattern recognition, pp. 1199–1208.
- Tang, H., Liu, X., Sun, S., Yan, X., Xie, X., 2021. Recurrent mask refinement for few-shot medical image segmentation, in: Proceedings of the IEEE/CVF International Conference on Computer Vision, pp. 3918–3928.
- Tian, Z., Zhao, H., Shu, M., Yang, Z., Li, R., Jia, J., 2020. Prior guided feature enrichment network for few-shot segmentation. IEEE transactions on pattern analysis and machine intelligence.
- Tomar, D., Lortkipanidze, M., Vray, G., Bozorgtabar, B., Thiran, J.P., 2021.

- Self-attentive spatial adaptive normalization for cross-modality domain adaptation. IEEE Transactions on Medical Imaging 40, 2926–2938.
- Wang, W., Xia, Q., Hu, Z., Yan, Z., Li, Z., Wu, Y., Huang, N., Gao, Y., Metaxas, D., Zhang, S., 2021. Few-shot learning by a cascaded framework with shape-constrained pseudo label assessment for whole heart segmentation. IEEE Transactions on Medical Imaging 40, 2629–2641.
- Weston, A.D., Korfiatis, P., Kline, T.L., Philbrick, K.A., Kostandy, P., Sakinis, T., Sugimoto, M., Takahashi, N., Erickson, B.J., 2019. Automated abdominal segmentation of ct scans for body composition analysis using deep learning. Radiology 290, 669–679.
- Xia, Y., Yang, D., Yu, Z., Liu, F., Cai, J., Yu, L., Zhu, Z., Xu, D., Yuille, A., Roth, H., 2020. Uncertainty-aware multi-view co-training for semisupervised medical image segmentation and domain adaptation. Medical Image Analysis 65, 101766.
- Yu, Q., Dang, K., Tajbakhsh, N., et al., 2021. A location-sensitive local prototype network for few-shot medical image segmentation, in: 2021 IEEE 18th International Symposium on Biomedical Imaging (ISBI), IEEE. pp. 262– 266.
- Zhang, C., Lin, G., Liu, F., Guo, J., Wu, Q., Yao, R., 2019. Pyramid graph networks with connection attentions for region-based one-shot semantic segmentation, in: Proceedings of the IEEE/CVF International Conference on Computer Vision.
- Zhao, A., Balakrishnan, G., Durand, F., Guttag, J.V., Dalca, A.V., 2019. Data augmentation using learned transformations for one-shot medical image segmentation, in: Proceedings of the IEEE/CVF conference on computer vision and pattern recognition, pp. 8543–8553.